Optimized Ferromagnetic Core Magnetorquer Design and Testing for LEO Nanosatellite Attitude Control

Gabriel Villalba-Alumbreros[1], Diego Lopez-Pascual[2], and Efren Diez-Jimenez[1]

[1]Mechanical Engineering Area, Signal Theory and Communications Department
Universidad de Alcalá, 28805, Madrid, Spain
gabriel.villalba@uah.es, efren.diez@uah.es

[2]Electrical Engineering Area, Signal Theory and Communications Department
Universidad de Alcalá, 28805, Madrid, Spain
d.lopezp@uah.es

Abstract – Magnetorquers are a very suitable solution for the nanosatellite's attitude and orbital control of low Earth orbit (LEO) given its constraints: small available volume, limited power consumption, and maximum weight limitation. In this work, an optimized ferromagnetic core magnetorquer is designed for LEO nanosatellites, considering the geometrical, electrical, and magnetic parameters in an electromagnetic finite element analysis (FEA). The final design dimensions are 10.9 mm diameter and 100 mm in length, with a ferromagnetic core made of high performance soft magnetic alloy Vacoflux50 measuring 5 mm diameter and 100 mm in length. Magnetorquer geometry has been optimized to achieve a very high compactness, reaching an optimal combination of high specific magnetic moment and magnetic moment-input power ratio at the same time. It shows a maximum magnetic moment of 1.42 Am^2, a magnetic moment-input power ratio of 2.52 Am^2/W, and a specific magnetic moment of 22.5 Am^2/kg, with a power consumption of 0.565 W and 0.5 A. Such a combination of high-performance values has not been previously found. Furthermore, it has displayed higher magnetic moment and specific magnetic moment than previous prototypes in literature. The simulated model is validated with the experimental testing of a manufactured prototype, by measuring the magnetic and electric variables.

Index Terms – attitude control, magnetic devices, magnetic rod, magnetorquer.

I. INTRODUCTION

Attitude control, stabilization and detumbling are some problems related to the position of any spacecraft in space around Earth [1]–[3]. For space applications, mechanical components with active moving parts can be used for attitude and vibration control [4]–[11]. However, they may suffer from reduced reliability as friction and wear may appear. On the other hand, magnetorquers are cheap, compact, reliable, and lightweight mechanical actuators without moving parts to control the orientation of the spacecraft [12].

Nanosatellites are constructed by only a 10 cm cube module or the junction of several cube modules, never exceeding 10 kg of total mass. In recent years, the development of this type of satellite has been increasing for commercial and military applications [13], including small satellite constellations [14]–[15]. This is due to plenty of new applications achievable with lower budgets and shorter development periods than those required for larger satellites.

A magnetorquer mainly consists of an electromagnet which produces a dipolar magnetic moment *m* when an electrical current flows through the winding. The magnitude of magnetic moment generated is mainly determined by the geometry, the magnetic properties of the materials and the circulating current. The square of the circulating current multiplied by the electrical resistance of the coil gives the power consumption of a magnetorquer, which is a significant performance parameter of this type of device. Depending on the size of the satellite, larger or smaller magnetic moment amounts are desired, and the smaller and lighter the magnetorquer is, the better for its integration in the satellite [16].

Magnetorquers interact with the Earth's magnetic field *B* producing a magnetic torque τ (Nm). It allows the satellite to rotate around its own center of mass. This relation is a vectorial product between *B* (T) and *m* (Am^2), as defined in equation (1):

$$\vec{\tau} = \vec{m} \times \vec{B} = |\vec{m}| \cdot |\vec{B}| \cdot \sin\theta. \tag{1}$$

Satellites located in low Earth orbit are subject to a more intense and uniform magnetic field compared to further away orbits. This is a requirement for the proper working of the magnetorquer, and it limits the use of

magnetorquers to LEO missions where the orbit has an altitude ranging from 200-300 km and up to 1600 km [17]. Hence, a magnetorquer designed for bigger satellites on further away orbits would have a lower torque-power ratio, given that the magnetic torque achievable with the same power consumption is lower.

The winding is made of low electrical resistivity materials such as copper or aluminum. Different coils can be manufactured depending on the size of the winding, from macro to micro size [18]–[19]. Its shape can vary from planar coreless square coils [20] to slender round iron-cored coils [21]. PCB printed planar coils are also used. The volume occupied by this kind of magnetorquer is very small and it also benefits the integration with its electronics [22]–[23]. Typically, different types of magnetorquer actuators are combined in an attitude control system for a suitable coordinated operation. In addition, systems like Helmholtz cages are used to test the mentioned system under controlled magnetic fields [24].

Iron-cored magnetorquers are especially interesting. The presence of a soft magnetic material core with a very high magnetic permeability increases the amount of magnetic moment generated [25]. Moreover, its low coercivity allows it to reduce the remanent magnetic moment when the coils are off. With these characteristics, more efficient designs are achievable. Nevertheless, the cylinder of the core tends to be very thin to minimize the demagnetization factor effects. The exact relation between the length of the core and its radius depends on the total size, and it can also be optimized.

The proposed iron-core magnetorquer in this work must fit in the nanosatellites volume, therefore, a maximum length of 100 mm for the magnetorquer is defined. The proposed design in this work, as it is optimized, reaches a combination of both high specific moment and magnetic moment-input power ratio, while maintaining a high magnetic moment and low power consumption. This combination of high values is not found in any previous magnetorquers found in literature.

In Table 1, some commercial and research magnetorquers with similar sizes are listed and compared. The total magnetic moment and relative specific and input power ratios are shown, giving some values of the goal performance.

In this paper an optimized iron-cored magnetorquer design is presented. In the following sections the theoretical model and its equations are defined. An electromagnetic parametric model in FEA software used for optimization is displayed. After the optimization, a detailed design is presented.

Finally, a prototype is manufactured, and a test setup is assembled to validate the FEA model with the present measurements.

Table 1: State-of-the-art of small magnetorquers

Length x Ø (mm x mm)	m (Am^2)	m/Power (Am^2/W)	m/I (Am^2/A)	m/Mass (Am^2/kg)	Ref
40x10.6	0.018	0.267	0.360	1.200	[26]-[27]
70x9	0.200	1.000	5.000	6.667	[28]
94x13	1.190	1.488	7.438	22.453	[29]
140x16	1.000	2.5	-	5	[30]
75x10	0.394	3.71	9.38	11.588	[31]

II. MAGNETORQUER DESIGN

The design of the magnetorquer is shown in Fig. 1. It consists of an inner cylindrical ferromagnetic core, fully winded with several overlapped layers of copper wire. The geometrical, electrical, and magnetic parameters are shown in Table 2. These parameters will be modified to find the optimal solution.

The materials properties also affect the performance, since the electrical power depends on the electrical resistivity of conductor, and the magnetic moment depends on the relative magnetic permeability of the core. In ferromagnetic materials, the desired properties are low coercivity (opposition to external field), high relative mag-
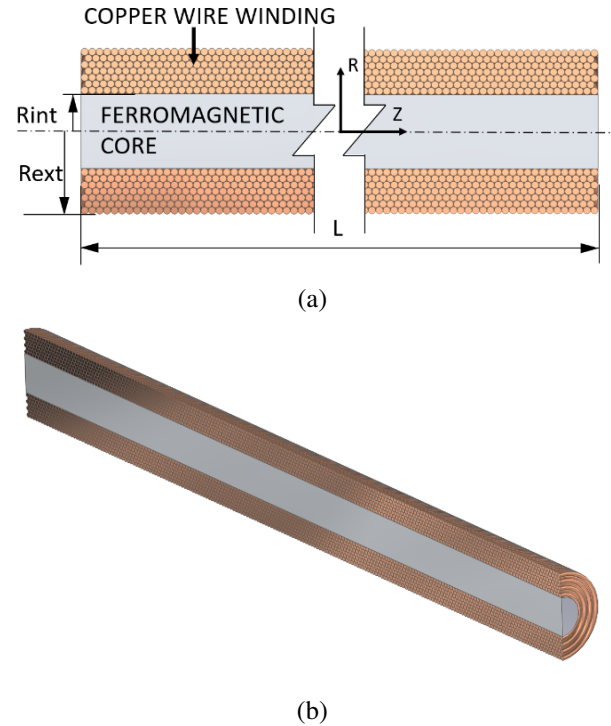

(a)

(b)

Fig. 1. (a) Magnetorquer elements and dimensional parameters and (b) 3D cross-section of the magnetorquer.

Table 2: Magnetorquer parameters

Symbol	Quantity
R_{int}	Core radius
R_{ext}	External winding radius
L	Length of the magnetorquer
D_{cable}	Wire diameter
mass	Device mass
I	Current
j	Current density
R	Electrical resistance
P	Power consumption
m	Magnetic moment

netic permeability (multiplication of external field), and high magnetic saturation (maximum field that can be stored inside the material). Among ferromagnetic materials, Fe-Co alloys present higher magnetic saturation than other alloys like Fe-Si or Ni-Fe. This means that a higher magnetic moment in less material is possible.

The material selected for the inner core is Vacoflux50® from the company VACUUM-SCHMELZE GmbH & Co, Hanau, Germany. Vacoflux50 showed one of the highest magnetic saturations on a machinable bar shape. According to the manufacturer, this material is composed of 49% Fe, 49% Co, 2% V + Nb. This material has been selected for its low coercivity (H_C = 100 A/m), high permeability (μ_r = 7000) and high saturation (B_{sat} = 2.3 T) [32].

To simplify the variable sweeping for the optimization in the design process, a solid copper body is considered instead of the series of layers of winding wire, as shown in Fig. 2. This simplification is possible, due to the fact that the magnetic field contribution to the core of a bare copper cylinder and a compact winding of wire copper is almost the same, because the conductor cross-section is nearly the same.

This simplification drives to equation 2, which correlates the total consumed power with the geometrical design parameters, the material conductivity and the current density applied. Equation 3 is included in the parametric FEA model to change the amount of copper of the magnetorquer depending on the electrical parameters
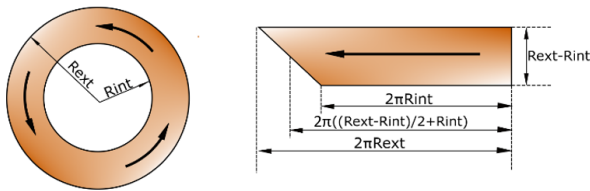
(current density and power) and geometrical parameters of the core (radius and length). The mass is calculated by using the density and the bulk of copper and iron core:

$$P = I^2 \cdot R = j^2 \cdot S^2 \cdot \rho \cdot \frac{L}{S}$$
$$= j^2 \cdot (R_{ext} - R_{int}) \cdot L \cdot \rho \cdot \pi \cdot (R_{ext} + R_{int}), \quad (2)$$

$$R_{ext} = \sqrt{\frac{P}{L \cdot \rho \cdot \pi \cdot j^2} + R_{int}^2}, \quad (3)$$

$$mass = L \cdot \pi \cdot \left(\rho_{copper} \cdot (R_{ext}^2 - R_{int}^2) + \rho_{alloy49} \cdot R_{int}^2 \right). \quad (4)$$

III. FINITE ELEMENT MODEL AND MAGNETIC MODEL CALCULATION

All calculations have been done using Ansys Electronics, a finite element model (FEM) software for simulation of electromagnetic fields. The magnetostatic field solution verifies Maxwell's equations:

$$\nabla \times \overrightarrow{H} = \overrightarrow{J}, \quad (5)$$

$$\nabla \cdot \overrightarrow{B} = 0, \quad (6)$$

with the following relationship applicable to each material:

$$\overrightarrow{B} = \mu_0 (\overrightarrow{H} + \overrightarrow{M}) = \mu_0 \cdot \mu_r \cdot \overrightarrow{H} + \mu_0 \cdot \overrightarrow{M}_p, \quad (7)$$

where H is the magnetic field intensity, B is the magnetic field density, J is the conduction current density, M_p is the permanent magnetization, μ_0 is the permeability of vacuum, and μ_r is the relative permeability of the core material [33].

The magnetostatic solver calculates the magnetic field distribution produced by combination of a known DC current density vector distribution and a spatial distribution of objects with magnetic properties. It is also needed to apply boundary conditions to the model, defining the limits of the environment of the simulation.

The design of the preliminary model for the FEM is shown in Fig. 3. It is an axisymmetric 2D model where the Z-axis is the axial symmetry axis. In this model, the geometrical parameters L and R_{int} can be modified

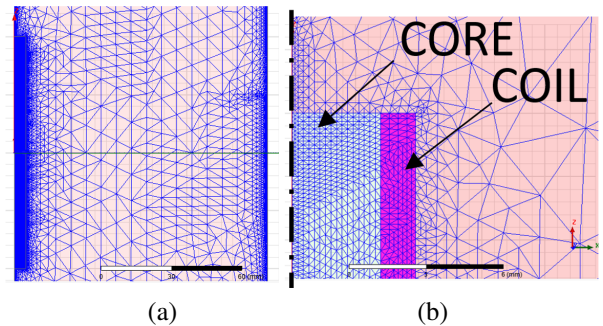Fig. 2. Magnetorquer simplified parametric model.

Fig. 3. (a) 2D axil-symmetrical model of the magnetorquer and (b) detail of the inner core and coil mesh.

parametrized. Mesh model size is proportional to the main geometrical parameters R_{int}, being finer in the surrounding interfaces. Triangular 2D elements have been considered.

A "Balloon" type boundary condition has been applied in the external edges. The Balloon condition models the region outside of the model space as being "infinitely" large. Moreover, an axisymmetric condition on the Z-axis has been imposed.

The external excitation of the model is a constant current density uniformly distributed in the copper coil cross-section, pointing perpendicularly towards the outside of the XZ plane. The value for this current density is $j = 4$ A/mm^2, common value for copper wires. The cross-section area corresponding with the coils is automatically modified by parametric modelling to adjust the specific power consumption. This is calculated using equation 3.

Materials considered in the simulation are the following: Vacoflux50, vacuum and copper. The defined properties for each of these materials are: magnetic permeability of vacuum, $\mu_0 = 4\pi \cdot 10^{-7}$H/m; relative permeability of copper, $\mu_{rCu} = 0.99991$; conductivity of copper at 20°C, $\sigma_{Cu} = 5.8 \cdot 10^7$ S/m; saturation of Vacoflux50 = 2.3 T; magnetic permeability of Vacoflux50 = 15000; and finally the B-H curve retrieved from the datasheet.

The main electromagnetic parameter that defines the behavior of the magnetorquer is the magnetic moment, m. The term magnetic moment normally refers to a system's magnetic dipole moment [34], the component of the magnetic moment that can be represented by an equivalent magnetic dipole: a magnetic north and south pole separated by a very small distance. In this article, we obtain the magnetic moment by postprocessing of the field density B measured in the axis of the magnetorquer at a certain distance from its center.

Two theoretical approximations have been used: uniformly magnetized core expression and magnetic dipole approximation. The expression to describe the magnetic field generated along the rotation axis by an uniformly magnetized core of length L is [25]:

$$B_z = \frac{m\,\mu_0}{4\pi}\left[\frac{\frac{z}{L}-\frac{1}{2}}{\left(z^2-zL+\frac{L^2}{4}\right)^{3/2}}-\frac{\frac{z}{L}+\frac{1}{2}}{\left(z^2+zL+\frac{L^2}{4}\right)^{3/2}}\right],$$

(8)

where z is the distance from the center of the core along the longitudinal Z-axis and m is the magnetic moment. Therefore, by using this expression, the magnetic moment can be determined if the simulation calculates the magnetic field B_z. This expression is useful since it does not require simulating and/or measuring the magnetic field far from the source. However, it assumes that the cylinder is uniformly magnetized which is not the case where the core is not fully saturated.

The magnetic dipole approximation correlates the generated magnetic field with the magnetic moment as:

$$B_z = \frac{\mu_0}{4\pi}\left[\frac{2m}{z^3}\right].$$

(9)

The magnetic dipole approximation is valid, provided that the considered magnetic field is far from the magnetic field source. As a rule of thumb, it is required to measure/simulate magnetic field at a distance more than 10 times the length of the magnetorquer.

In post-processing, we have calculated the magnetic moment simultaneously at different distances and with two different methods. The value of the magnetic moment used for the study is the average between the two methods at $z = 0.75$ m. This distance is enough to consider that the average value is stabilized for the maximum length of 10 cm with a tolerable error.

IV. GEOMETRY OPTIMIZATION FOR MAXIMUM PERFORMANCE

A geometry optimization process to define the best performing geometric combination has been carried out. The electromagnetic simulation is performed for steady state conditions. Dynamic behavior is not considered, nevertheless, non-linearities on Earth's magnetic field, changes on orientation commands, and detumbling problems need to be considered during operation. Several techniques have been developed using inertial measurement units [35].

The objective of the optimization is to maximize specific magnetic moment and magnetic moment-input power ratio at the same time. The output variables are total magnetic moment, specific magnetic moment (magnetic moment/mass) and magnetic moment-input power ratio (magnetic moment/power). In the first optimization step, input variables are length L and radius of the core R_{int}.

The dimensions have been limited to ranges from 10 to 100 mm in length and from 1 to 15 mm in radius, which are typical values of commercial magnetorquers. We have performed the simulation for 0.3 and 3 W, typical available power levels in satellites. Having the power as a constraint, and fixing a maximum current density, equation (3) returns a value of R_{ext} by selecting L and R_{int}.

Figure 4 shows the total magnetic moment for different combinations of length and core radius applying a power of 0.3 W. It can be observed that the total magnetic moment is larger for longer magnetorquers and for smaller core radius. This makes sense since demagnetizing factors are more severe for larger R/L ratios, i.e., thicker cylinders, than for slim cylinders. In any case, the longer the cylinder is, the larger its total magnetized
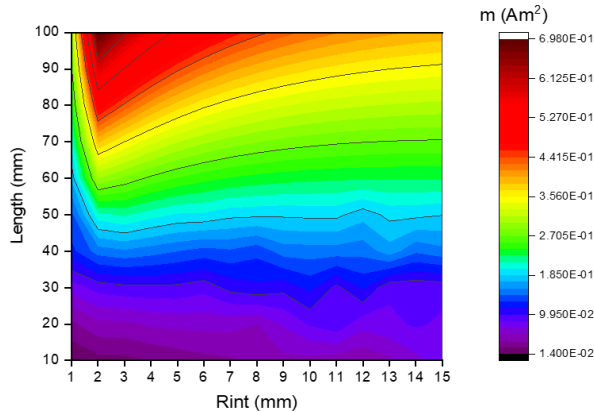
Fig. 4. Magnetic moment for different length and core radius, power P=0.3 W.
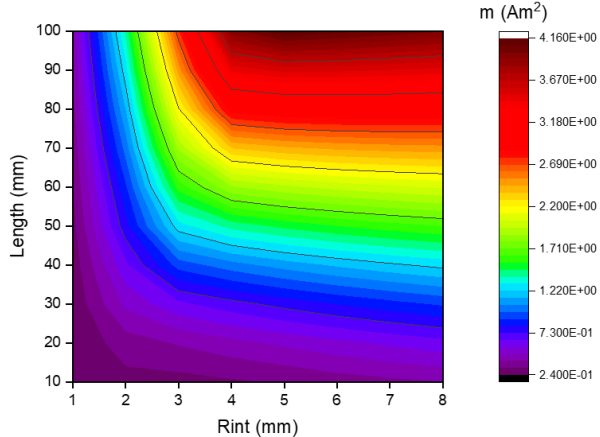

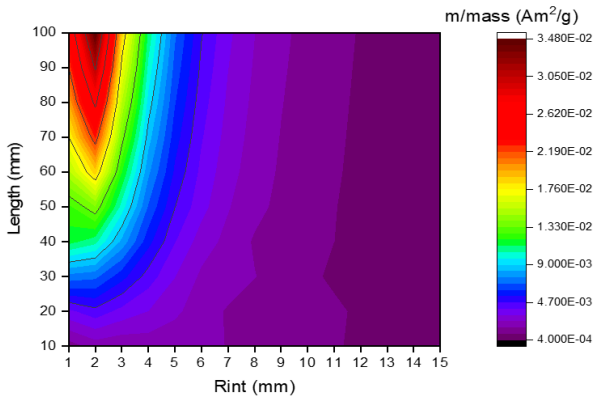Fig. 6. Magnetic moment for different length and core radius, power P=3 W.

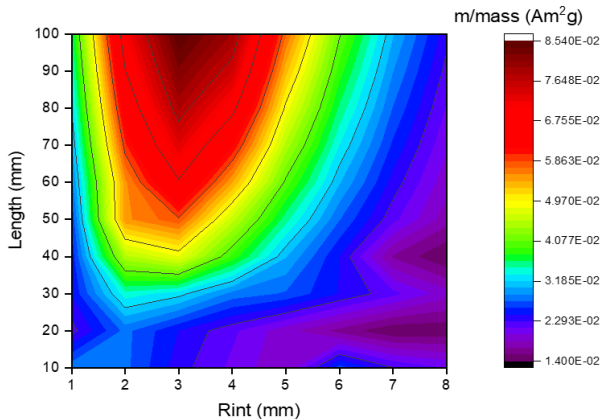Fig. 5. Specific magnetic moment for different length and core radius, power P=0.3 W.

Fig. 7. Specific magnetic moment for different length and core radius, power P=3 W.

mass will be, and thus the larger its magnetic moment, even for the same power applied.

Figure 5 shows the specific magnetic moment for different combinations of length and core radius. The effect of the demagnetizing factor is even more pronounced for this parameter. The longer and thinner the magnetorquer, the more optimized in compactness (m/mass) it is.

The same analysis has been done for a power of 3 W, with similar results, as shown in Figs. 6 and 7. After this first optimization analysis, we determined that $L = 100$ mm is the optimal length in terms of specific magnetic moment for both levels of power.

To fix the core radius, different comparisons have been done from previous simulation results for $L = 100$ mm. Figure 8 shows a comparison of the total magnetic moment values for the two levels of power.

As expected, the magnetic moment is larger for a higher power, since more power also implies a larger current, and thus more magnetization is achieved in the vol-
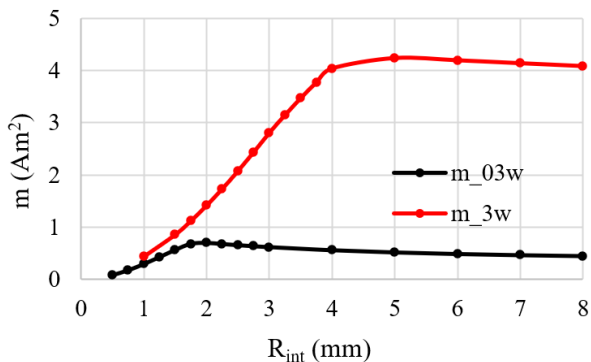

Fig. 8. Magnetic moment comparison for power 0.3 and 3 W with a fixed length of 100 mm.

ume. But it can be observed that the maximum of the magnetic moment is achieved in different core radius values for each power level. More specifically, for a power of 0.3 W, the maximum is achieved at around

2 mm of radius; for 3 W, this maximum is achieved at 4 mm.

Regarding the compactness of the magnetorquer, the behavior reverses. As shown in Fig. 9, the magnetorquer provides a larger specific magnetic moment for a lower level of power. This can be explained by the fact that, for larger power, there are some areas of the magnetorquer that get saturated, so they do not proportionally contribute for larger magnetic fields. Again, maximums are found at between 2 and 4 mm.

The last analyzed parameter is the ratio between the magnetic moment and the corresponding power consumption to obtain it. Figure 10 shows the ratio for both levels of power and for different core radius. It is more efficient when operating at 0.3 W than at 3 W, getting the maximum value again at 2 mm for 0.3 W and at 4 mm for 3 W. It shows that maximum achievable magnetic moment-input power ratio is reduced when the applied electric power increases for any size of core diameter in the evaluated range of 0.3-3 W, contrary to the magnetic moment generation.

Therefore, for an operation ranging between 0.3 and 3 W, an optimal value for the core radius will be located
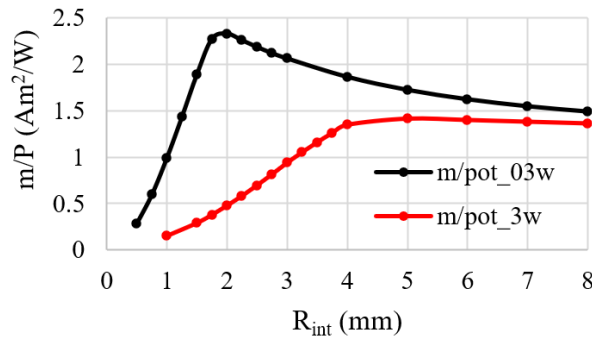
Table 3: Magnetorquer design for several power levels

Power (W)	R_{ext} (mm)	m (Am^2)	m/Power (Am^2/W)	m/Mass (Am^2/kg)
0.1	2.72	0.24	2.35	12.00
0.3	3.12	0.65	2.18	25.24
0.75	3.87	1.44	1.92	35.55
1	4.23	1.81	1.81	37.16
3	6.42	2.97	0.99	25.97
10	11.07	3.75	0.38	10.92

between 2 and 4 mm. From this optimization analysis, we have set the core radius to be R_{int} = 2.5 mm, as a tradeoff between 0.3 and 3 W of power. This value optimizes both specific moment (m/mass) and magnetic moment/power ratio (m/power) giving a unique combination of high compactness never found previously in literature.

The value of the external radius R_{ext} is related to the amount of power that the magnetorquer is thought to handle. Table 3 shows the different values of external radius needed to handle several levels of power, maintaining a current density value of 4 A/mm^2, and the specific and magnetic moment-input power ratio performance variables obtained. Between 3.87 mm and 6.42 mm of external radius high magnetic moment and maximum specific moment in mass and power have been found. Finally, a value of 5 mm has been selected since it allows higher levels of moment while reaching maximum values of specific magnetic moment.

V. FINAL DESIGN DESCRIPTION AND FEM ANALYSIS

Once the dimensional parameters of the simplified model are fixed, several wire diameter configurations have been simulated for a constant current density of 4 A/mm^2. An analytical expression has been used to predict the total length of the wire considering an overlapping configuration between layers. This led to a more realistic resistance calculus, which depends on wire geometry:

$$L_{Cable} = f(L, n, D_{Cable}) = \frac{L}{D_{Cable}} 2\pi \cdot n_i \cdot$$
$$(R_{int} + D_{Cable}(0.866 \cdot n_i - 0.366))$$
$$+ \left(\frac{L}{D_{Cable}} - 1\right) 2\pi \cdot n_p \cdot \qquad (10)$$
$$(R_{int} + D_{Cable}(0.866 \cdot n_p + 0.5))).$$

In terms of total consumed power, generated magnetic moment, and transient time constant, there are no significant changes when the diameter of the wire varies. In Fig. 11, a comparative of the simulation for different wire diameters is shown, where the impact of the filling factor of the winding is visible. Nevertheless, the
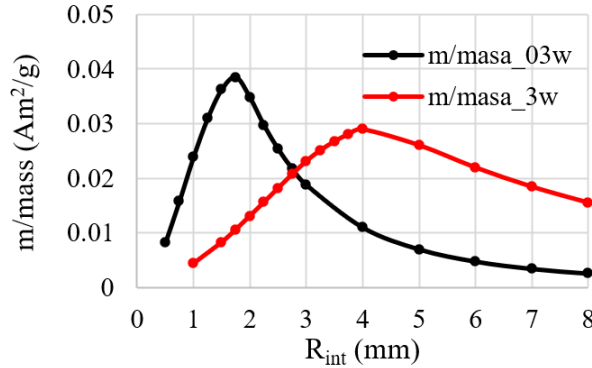

Fig. 9. Specific magnetic moment comparison for power 0.3 and 3 W with a fixed length of 100 mm.

Fig. 10. Magnetic moment/power ratio comparison for power 0.3 and 3 W with a fixed length of 100 mm.
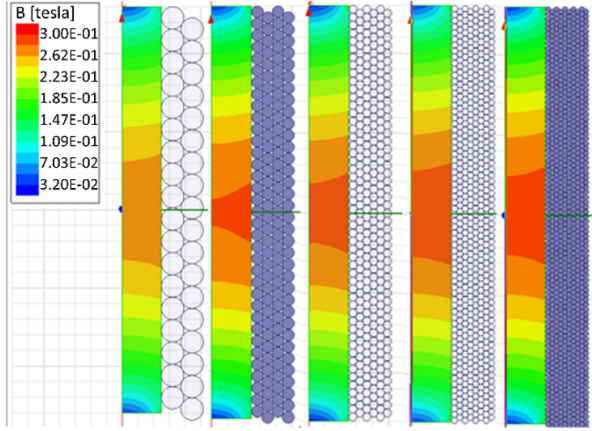
Fig. 11. Simulation of field density in the core for different bare wire diameters.

resistance and the voltage increase as the wire gets thinner, as well as the flowing current decreases. Another consideration that must be taken account is the dynamic behavior of the device. It is adjustable by varying the number of layers and wire diameter, without altering the steady state value. Calculations show that the inductance and resistance of the design ranges from 0.94 uH and 0.0092 Ω (for 2 layers) to 440 uH and 4.865 Ω (for 6 layers). Electronic elements as resistors, inductors or capacitors can be added to adjust the dynamic response too.

The selection of the wire is a compromise between manufacturing feasibility and electrical compatibility. Use of larger wires results in an easier manufacturing process, since for very small wires the control of the layers is more complex. In addition, the electronic systems mounted on the satellite are cheaper and easier to integrate when lower levels of current are needed.

The selected diameter has been a compromise between appropriate levels of current and feasibility on manufacturing, choosing 6 layers for 0.5 mm of wire diameter and 200 turns per layer. Considering the protecting varnish of the real cable the number of turns is corrected to 180, and the external radius to 5.45 mm. In Table 4, the configuration and the operation ranges of the detailed final design are shown.

The detailed model has been simulated varying the input current. The results show the average magnetic saturation level inside the ferromagnetic core. In Fig. 12 it can be observed that, between 0.75 A and 1 A, there is a value of current from which the core starts saturating. It means that the magnetic moment gained from that point is mostly due to vacuum magnetic permeability rather than the permeability of the core material, the moment-current ratio drops from a constant value and stars decreasing, as Fig. 13 shows.

Table 4: Magnetorquer final design parameters

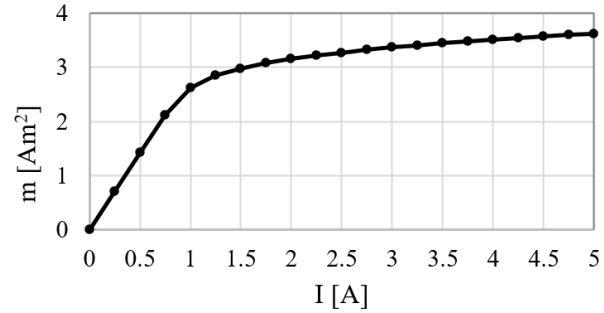|	
R_{int} (mm)	2.5
R_{ext} (mm)	5.45
L (mm)	100
D_{cable} (mm)	0.5
Mass (g)	63.26
R (ohm)	2.26
I (A)	1.15
P (W)	0.3-3
R_{int} (mm)	2.5

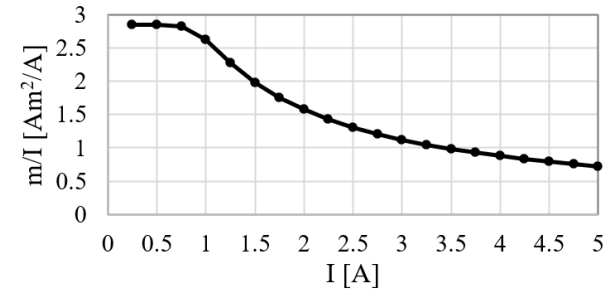Fig. 12. Magnetic moment as function of the applied current.

Fig. 13. Magnetic moment sensitivity with current as function of the applied current.
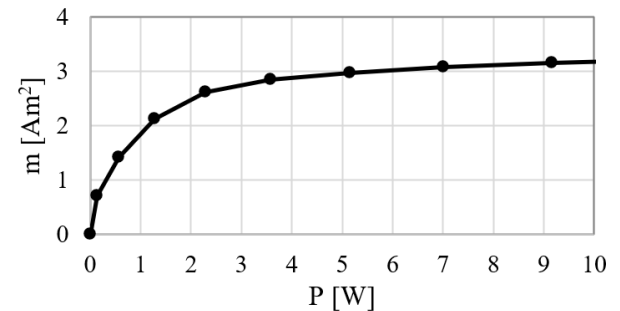

Fig. 14. Magnetic moment as function of the applied power.

In the case of the power, rapidly the saturation point is reached near to 4 W, as shown in Fig. 14, because

power is function to the square of the current. The best operation range for the device in terms of magnetic moment-input power ratio is the 0.3-3 W range. However, increasing the power when the core is close to saturation worsens this ratio, but it still gives more absolute magnetic moment.

Table 5: Magnetorquer operation working points

P (w)	0.3	0.565	3
I (A)	0.36	0.5	1.15
m (Am^2)	1.02	1.42	2.76
m/Power (Am^2/W)	3.4	2.52	0.92
m/I (Am^2/A)	2.83	2.85	2.4
m/Mass (Am^2/kg)	16.12	22.5	43.63

In Table 5, values of magnetic moment, magnetic moment-input power ratio, and specific moment are shown for various operation working points, including operation limits. Compared with Table 1, for the lower power limit of operation, the magnetic moment-input power ratio is higher than commercial products, but the specific moment is low. In contrast, the upper power limit of operation presents a higher specific moment than the commercial products, but the magnetic moment-input power ratio is low. A trade-off operation point of 0.565 W and 0.5 A is selected. It presents higher values of magnetic moment and specific moment than all the state-of-the-art (SOA) magnetorquers presented in Section I. If the input power is reduced to 0.3 the magnetic moment-power ratio reaches more than 91% of the maximum power found in literature. The comparison between SOA and this work is shown in Table 6.

Electromagnetic contamination of the magnetorquer at any point in space can be directly obtained by using the magnetic dipolar moment approximation once it is known the effective magnetic moment. Requirements for EMC shielding can be designed from these calculations.

Table 6: Comparison between magnetorquers of SOA and this work

Length x Ø (mm x mm)	m (Am^2)	m/Power (Am^2/W)	m/I (Am^2/A)	m/Mass (Am^2/kg)	Ref.
40x10.6	0.018	0.267	0.360	1.200	[26]-[27]
70x9	0.200	1.000	5.000	6.667	[28]
94x13	1.190	1.488	7.438	22.453	[29]
140x16	1.000	2.5	-	5	[30]
75x10	0.394	3.71	9.38	11.588	[31]
100x10.9	1.42	2.52	2.85	22.5	This work

VI. PROTOTYPE MANUFACTURING AND EXPERIMENTAL SET-UP

A prototype has been manufactured to validate the FEA electromagnetic model of the design. A 5 mm diameter and 100 mm long core of Vacoflux50 was machined in a lathe. The rod was made with small holes on its ends for assembling the retainers. These removable glued support parts allow a correct axial alignment between the Hall-effect probe and the magnetorquer in the measurements. In addition, it helps to ensure a correct compactness between turns during the winding process.

A 0.5 mm diameter enameled copper wire has been used for making the windings. Due to the thickness of the protective layer of wires, the filling factor has been reduced from 200 turns per layer to 180 turns per layer as predicted. Through the length of wire used and the unitary resistance of the wire, the resistance of the winding can be predicted. Furthermore, the resistance of the final winding was measured with an LRC impedance measuring device, showing a value of 2.291 Ω. This ensures that the number of turns in the winding, its disposition and resistance accomplish the predicted values. The final prototype is shown in Fig. 15.
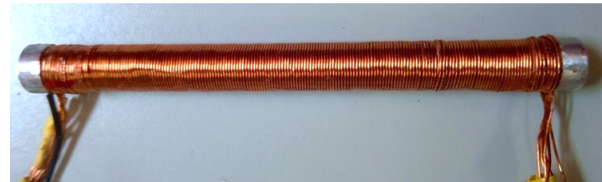

Fig. 15. Manufactured prototype.

The connections between layers were made in series so that it was possible to apply the same current through all the layers. For that purpose, a connection PCB board with neglectable resistance was made through micro-CNC machining process. Afterwards, the terminals were welded to the board.

The experimental set up assembled for the measurements consists of a voltage supply (EX355P-USB from AIM-TTI INSTRUMENTS) and a magnetic field Hall-effect sensor (GM08 from Hirst Magnetics) which measures the axial magnetic field density with an axial probe. The voltage source also measures consumed current.

The magnetorquer is fixed to an aluminum base through aluminum brackets, keeping it away from any magnetic material so as to not contaminate the measurement space. The probe is set in the aluminum retainer and fixed with another backet. The final assembly is shown in Fig. 16. The probe the magnetorquer keeps aligned, with a controlled distance of 5 mm to the end of the magnetorquer.
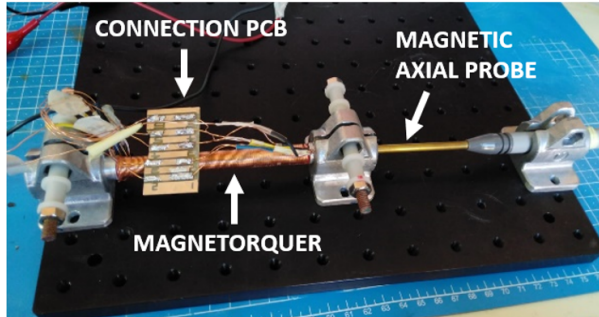
Fig. 16. Magnetorquer and probe assembly set up.

Once the setup is mounted, several measurements at different voltage points have been done. The comparison has been made through the magnetic field-current curve, considering the measurement distance. The distance between the center of the magnetorquer to the Hall-effect transducer of the probe is 55.5 mm. That is the distance to be considered for the validation of the prototype and the later calculation of the magnetic moment.

The measurement must be done as close as possible to the end of the magnetorquer, since with increasing distances the field intensity gets lower, and misalignment or distance errors are more likely to occur.

VII. TEST RESULTS AND DISCUSSION

The validation of the prototype has been achieved through the magnetic field density measurement in the FEA electromagnetic model, measured at the same axial distance. After validation, the magnetic moment can be calculated at a further distance measuring the field in the simulation model.

In Fig. 17, the comparison between testing measurements and simulation for two configurations is presented. At lower magnetic field levels, such as a 3-layer configu-
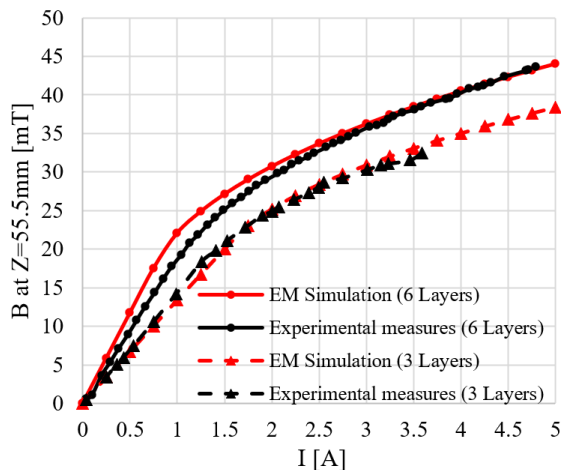

Fig. 17. Generated magnetic field as function of current.

ration, in the mostly linear behavior, the simulation curve perfectly fits the experimental measures. The difference between the two curves in the 6-layer case is caused by a change in the magnetic properties of the ferromagnetic material. This change at higher magnetic field levels can be produced by the effect of the heat generation during operation while measuring. However, the model is validated and it is demonstrated that the prototype has the expected specifications of the design and the electromagnetic model.

VIII. CONCLUSION

A magnetorquer, as any other spacecraft subsystem, has very strict constraints in terms of mass, volume, and power consumption. An optimized iron-core magnetorquer prototype for LEO nanosatellites is presented in this work.

The design process starts with the definition of a conceptual design with its own variables. A simplified design, with a context of parameters, equations and limitations, is established. Through an electromagnetic finite element analysis (FEA) model, the parametric optimization has been done. Using both the electrical and geometrical parameters, the optimization had the objective of achieving values as high as possible of magnetic moment, specific moment, and moment.

After the simplified model is optimized, a detailed design is presented. The design achieves a combination of magnetic moment, magnetic moment-input power ratio and specific moment values not found in the state of the art. The magnetorquer proposed in this work has 100 mm length and 10.9 mm diameter, with a ferromagnetic core made of Vacoflux50 with 5 mm diameter. The wire is an enameled copper wire with 0.5 mm bare copper diameter.

The operation condition range studied for the device is from 0.3 W (0.36 A) to 3 W (1.15 A). The optimized working point has been found to be at 0.565 W (0.5 A). At this point the values reached are: 1.42 Am^2, 2.52 Am^2/W, and 22.5 Am^2/kg. Magnetorquer geometry has been optimized to achieve a very high compactness, reaching an optimal combination of high magnetic moment, specific magnetic moment, and magnetic moment-input power ratio at the same time. Such a combination of high-performance values has not been found in the literature before with iron-cored magnetorquers. The value of magnetic moment and specific magnetic moment is higher than found on earlier prototypes in the literature.

Finally, to validate the model, a prototype has been manufactured, as well as a test setup. In the test setup, measurements of magnetic field density, voltage, current and resistance have been done without considering thermal effects, which will have to be evaluated in a relevant

environment in future work. As the simulated and experimental values were in good agreement, the FE model of the prototype is validated.

REFERENCES

[1] Y. Gu, Q. Liang, S. Wang, A. Zhou, and C. Liu, "Shape optimization of the momentum ring cross section for satellite attitude control based on magnetohydrodynamics," *Applied Computational Electromagnetics Society (ACES) Journal*, vol. 37, no. 3, pp. 348-353, 2022.

[2] F. Mesch, "Magnetic components for the attitude control of space vehicles," *IEEE Trans. Magn.*, vol. 5, no. 3, pp. 586-592, 1969.

[3] K. R. Rajagopal, "Design and development of a permanent magnet torquer for a gyroscope," *IEEE Trans. Magn.*, vol. 37, no. 4, pp. 2630-2633, 2001.

[4] M. Tang, J. Zhou, C. Jin, and Y. Xu, "Vibration isolation of magnetic suspended platform with double closed-loop PID control," *Applied Computational Electromagnetics Society (ACES) Journal*, vol. 32, no. 8, pp. 712-719, 2017.

[5] R. Alcover-Sanchez, J. M. Soria, J. Pérez-Aracil, E. Pereira, and E. Diez-Jimenez, "Design and experimental characterization of a novel passive magnetic levitating platform," *Smart Struct. Syst.*, vol. 29, no. 3, pp. 499-512, 2022.

[6] E. Diez-Jimenez, C. Alén-Cordero, R. Alcover-Sánchez, and E. Corral-Abad, "Modelling and test of an integrated magnetic spring-eddy current damper for space applications," *Actuators*, vol. 10, no. 1, 2021.

[7] M. Muñoz-Martínez, E. Diez-Jimenez, M. J. Gómez-García, R. Rizzo, and A. Musolino, "Torque and bearing reaction forces simulation of micro-magnetic gears," *Applied Computational Electromagnetics Society (ACES) Journal*, vol. 34, no. 4, pp. 541-546, 2019.

[8] E. Diez-Jimenez, R. Sanchez-Montero, and M. Martinez-Muñoz, "Towards miniaturization of magnetic gears: Torque performance assessment," *Micromachines*, vol. 9, no. 1, p. 16, Dec. 2017.

[9] F. Fiorillo, F. Santoni, E. Ferrara, M. L. Battagliere, O. Bottauscio, and F. Graziani, "Soft magnets for passive attitude stabilization of small satellites," *IEEE Trans. Magn.*, vol. 46, no. 2, pp. 670-673, Feb. 2010.

[10] J. Esnoz-Larraya, I. Valiente-Blanco, C. Cristache, J. Sanchez-Garcia, F. Celis, E. Diez-Jimenez, and J. L. Perez-Diaz. "OPTIMAGDRIVE: High performance magnetic gears development for space applications," in *17th European Space Mechanisms and Tribology Symposium*, pp. 1-5, 2017.

[11] J. Perez-Diaz, E. Diez-Jimenez, I. Valiente-Blanco, C. Cristache, and J. Sanchez-Garcia-Casarrubios, "Contactless mechanical components: Gears, torque limiters and bearings," *Machines*, vol. 2, no. 3, pp. 312-324, 2014.

[12] D. S. Ivanov, M. Y. Ovchinnikov, V. I. Penkov, D. S. Roldugin, D. M. Doronin, and A. V. Ovchinnikov, "Advanced numerical study of the three-axis magnetic attitude control and determination with uncertainties," *Acta Astronaut.*, vol. 132, pp. 103-110, Mar. 2017.

[13] T. Wekerle, J. B. P. Filho, L. E. V. L. da Costa, and L. G. Trabasso, "Status and trends of smallsats and their launch vehicles - An up-to-date review," *J. Aerosp. Technol. Manag.*, vol. 9, no. 3, pp. 269-286, 2017.

[14] T. Inamori, R. Kawashima, P. Saisutjarit, N. Sako, and H. Ohsaki, "Magnetic plasma deorbit system for nano- and micro-satellites using magnetic torquer interference with space plasma in low Earth orbit," *Acta Astronaut.*, vol. 112, pp. 192-199, 2015.

[15] J. H. Park, S. Matsuzawa, T. Inamori, and I. S. Jeung, "Nanosatellite constellation deployment using on-board magnetic torquer interaction with space plasma," *Adv. Sp. Res.*, vol. 61, no. 8, pp. 2010-2021, 2018.

[16] A. Ali, M. R. Mughal, H. Ali, L. M. Reyneri, and M. N. Aman, "Design, implementation, and thermal modeling of embedded reconfigurable magnetorquer system for nanosatellites," *IEEE Trans. Aerosp. Electron. Syst.*, vol. 51, no. 4, pp. 2666-2679, 2015.

[17] C. S. Allen, M. Giraudo, C. Moratto, and N. Yamaguchi, "Spaceflight environment," in *Space Safety and Human Performance*, T. Sgobba, B. Kanki, J.-F. Clervoy, and G. M. Sandal, Eds. Amsterdam: Elsevier, pp. 87-138, 2017.

[18] M. Martinez-Muñoz, E. Diez-Jimenez, G. V. Villalba-Alumbreros, M. Michalowski, and A. Lastra-Sedano, "Geometrical dependence in fixtures for 2D multipole micromagnets magnetization pattering," *Applied Computational Electromagnetics Society (ACES) Journal*, vol. 34, no. 7, 2019.

[19] M. Martinez-Muñoz, E. Diez-Jimenez, R. Sanchez-Montero, P. L. Lopez-Espi, and J. A. Martinez-Rojas, "Analysis of the geometric parameters influence in PCB fixtures for 2D multipole magnetization patterning of thin layer micro-magnets," *Int. J. Appl. Electromagn. Mech.*, vol. 61, no. 1, 2019.

[20] G. Cervettini, S. Pastorelli, H. Park, D. Y. Lee, and M. Romano, "Development and experimentation of a CubeSat magnetic attitude control system testbed," *IEEE Trans. Aerosp. Electron. Syst.*, vol. 57, no. 2, pp. 1345-1350, 2021.

[21] M. Fakhari Mehrjardi and M. Mirshams, "Design and manufacturing of a research magnetic torquer rod," *Fourth Int. Conf. Exp. Mech.*, vol. 7522, no. 5, p. 75221W, 2009.

[22] M. R. Mughal, H. Ali, A. Ali, J. Praks, and L. M. Reyneri, "Optimized design and thermal analysis of printed magnetorquer for attitude control of reconfigurable nanosatellites," *IEEE Trans. Aerosp. Electron. Syst.*, vol. 56, no. 1, pp. 736-747, 2020.

[23] N. J. Sorensen, "Efficiency-optimized design of PCB-integrated magnetorquers for CubeSats," *IEEE Trans. Aerosp. Electron. Syst.*, vol. 57, no. 6, pp. 3623-3632, 2021.

[24] R. C. Da Silva, I. S. K. Ishioka, C. Cappelletti, S. Battistini, and R. A. Borges, "Helmholtz cage design and validation for nanosatellites HWIL testing," *IEEE Trans. Aerosp. Electron. Syst.*, vol. 55, no. 6, pp. 3050-3061, 2019.

[25] J. Lee, A. Ng, and R. Jobanputra, "On determining dipole moments of a magnetic torquer rod - Experiments and discussions," *Can. Aeronaut. Sp. J.*, vol. 48, no. 1, pp. 61-67, 2002.

[26] G. P. Candini, F. Piergentili, and F. Santoni, "Designing, manufacturing, and testing a self-contained and autonomous nanospacecraft attitude control system," *J. Aerosp. Eng.*, vol. 27, no. 6, p. 04014033, 2014.

[27] G. P. Candinia, F. Piergentilib, and F. Santoni, "Miniaturized attitude control system for nanosatellites," *Acta Astronaut.*, vol. 81, no. 1, pp. 325-334, 2012.

[28] "CubeSatShop Cubesat NCTR-M002 magnetic rod," Datasheet.

[29] "CubeSatShop Cubesat NCTR-M012 magnetic rod," Datasheet.

[30] "Sputnix SX-MT Magnetic Torquers," Datasheet.

[31] H. Ali, M. R. Mughal, Q. ul Islam, M. R. Anjum, S. Ishaq, and L. M. Reyneri, "Parametric optimization and analysis of power efficient magnetorquer rod actuator for nanosatellite," *IEEE J. Miniaturization Air Sp. Syst.*, vol. 3, no. 2, pp. 30-35, 2022.

[32] "Vaccumshmeltze: Iron-cobalt alloys," Datasheet.

[33] "Ansoft Ansys Maxwell v15 - Help assistant," Datasheet, 2018.

[34] Y. Yu, H. Yue, F. Yang, H. Zhao, and Y. Lu, "Electromagnetic interaction between a slowly rotating conducting shell and magnetic dipoles: A theoretical and numerical study," *IEEE Trans. Magn.*, vol. 57, no. 8, 2021.

[35] D. M. Torczynski, R. Amini, and P. Massioni, "Magnetorquer based attitude control for a nanosatellite testplatform," *American Institute of Aeronautics and Astronautics*, 2010.

Gabriel Villalba-Alumbreros received his M.Sc. in Industrial Engineering in 2022 and B.Sc. in Electronics and Industrial Automation Engineering in 2019. Currently he is working in UWIPOM2 project under Horizon 2020 EU funding programme for research and innovation at University of Alcalá. His research interests are focused in electromagnetic actuators, mechatronic systems, MEMS and control systems.
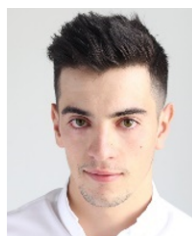
Diego López-Pascual is an Assistant Professor at the Electrical Engineering area of Universidad de Alcalá. He obtained his Ph.D. on Industrial Engineering in 2023. He joined the Mechanical, Electric & Thermal Technologies research group at Universidad de Alcalá at the beginning of 2020, where he is working on the UWIPOM2 project under EU funding. His main research interests are industrial design, thermal characterization of systems, and renewable energy systems modelling, subject on which his Ph.D. was developed.

Efrén Díez-Jiménez is a Professor at the Mechanical Engineering area of Universidad de Alcalá. He obtained his Ph.D. on Mechanical Engineering and Industrial Organization in 2012, M.Sc. on Machines and Transport Engineering in 2010 and Bachelor on Industrial Engineering in 2008 from Universidad Carlos III de Madrid, Spain. In 2013, he received the Extraordinary Award for the Best Thesis in Mechanical Engineering. He has participated as coordinator into different ESA-H2020-FP7 projects with successful results. Currently, he is coordinator of H2020 European project UWIPOM2, where micro-robotic rotary actuators are being developed. Author of more than 35 articles and 5 patents granted, he also collaborates as reviewer in mechanical engineering journals. His main research interests are mechanisms and machine design, electromagnetic actuators and MEMS.